

ARTICLE

Received 24 Dec 2014 | Accepted 14 May 2015 | Published 26 Jun 2015

DOI: 10.1038/ncomms8507

OPEN

# Hyperbolic phonon-polaritons in boron nitride for near-field optical imaging and focusing

Peining Li<sup>1</sup>, Martin Lewin<sup>1,2</sup>, Andrey V. Kretinin<sup>3</sup>, Joshua D. Caldwell<sup>4</sup>, Kostya S. Novoselov<sup>3</sup>, Takashi Taniguchi<sup>5</sup>, Kenji Watanabe<sup>5</sup>, Fabian Gaussmann<sup>2</sup> & Thomas Taubner<sup>1,2</sup>

Hyperbolic materials exhibit sub-diffractive, highly directional, volume-confined polariton modes. Here we report that hyperbolic phonon polaritons allow for a flat slab of hexagonal boron nitride to enable exciting near-field optical applications, including unusual imaging phenomenon (such as an enlarged reconstruction of investigated objects) and sub-diffractive focusing. Both the enlarged imaging and the super-resolution focusing are explained based on the volume-confined, wavelength dependent propagation angle of hyperbolic phonon polaritons. With advanced infrared nanoimaging techniques and state-of-art mid-infrared laser sources, we have succeeded in demonstrating and visualizing these unexpected phenomena in both Type I and Type II hyperbolic conditions, with both occurring naturally within hexagonal boron nitride. These efforts have provided a full and intuitive physical picture for the understanding of the role of hyperbolic phonon polaritons in near-field optical imaging, guiding, and focusing applications.

<sup>1</sup>Institute of Physics (IA), RWTH Aachen University, Aachen 52056, Germany. <sup>2</sup>Fraunhofer Institute for Laser Technology ILT, Aachen 52074, Germany. <sup>3</sup>School of Physics and Astronomy, University of Manchester, Oxford Road, Manchester M13 9PL, UK. <sup>4</sup>US Naval Research Laboratory, 4555 Overlook Avenue, S.W., Washington, D.C. 20375, USA. <sup>5</sup>National Institute for Materials Science, 1-1 Namiki, Tsukuba, Ibaraki 305-0044, Japan. Correspondence and requests for materials should be addressed to J.D.C. (email: joshua.caldwell@nrl.navy.mil) or to Th.T. (taubner@physik.rwth-aachen.de).

The propagation of sub-diffractive waves in hyperbolic media<sup>1</sup> enables many unusual optical possibilities such as hyperlensing<sup>2–4</sup>, negative refraction<sup>5,6</sup>, enhanced quantum radiation<sup>7</sup>, nanolithography<sup>8</sup> and sub-diffractive resonators<sup>9,10</sup>. Very recently, it was demonstrated that the highly directional propagation of volume-confined, hyperbolic polaritons (HPs) is key for these sub-diffractive phenomena<sup>8,10,11</sup>. Their directionality derives from the sign and magnitude of the two principal (in- and out-of-plane) components of the dielectric-permittivity tensor ( $\vec{\epsilon} = \text{diag}[\epsilon_{xx}, \epsilon_{yy}, \epsilon_{zz}]$ ), which have opposite signs in hyperbolic materials. The propagation angle  $\theta$  (for example, the angle between the Poynting vector and the  $z$  axis) of the HPs in hyperbolic media can be roughly approximated as<sup>10</sup>,

$$\theta = \pi/2 - \arctan\left(\sqrt{\epsilon_z(\omega)}/i\sqrt{\epsilon_t(\omega)}\right) \quad (1)$$

where  $\epsilon_t = \epsilon_{xx} = \epsilon_{yy}$  and  $\epsilon_z = \epsilon_{zz}$  are the in- and out-of-plane dielectric permittivities of the hyperbolic medium, respectively. Therefore, by controlling the ratio of the two principal dielectric components, the propagation direction of the HPs can be tuned.

Until very recently, hyperbolic media have been explored through man-made hyperbolic metamaterial (HMM) structures, such as metal-dielectric multilayers<sup>4,5</sup>, nanowire<sup>6,12</sup> or nanopillar arrays<sup>9</sup> embedded within a dielectric medium. In HMMs, the effective dielectric permittivities are determined by the geometric parameters of their subwavelength unit cells<sup>1</sup>. As such, the maximum wavevector  $\mathbf{k}$  that can be induced to propagate through the material is limited by the size of the artificial unit cell. This in turn limits the degree of optical confinement and spatial resolution that can be realized. Furthermore, the high losses associated with noble metals<sup>13–15</sup> used in man-made HMM structures result in short propagation lengths, quite broad resonance linewidths and in terms of hyperlens designs, low transmission efficiency.

During the search for better plasmonic materials<sup>14,15</sup>, polar dielectrics capable of supporting phonon-polaritons such as silicon carbide<sup>16–20</sup> and hexagonal boron nitride (hBN)<sup>10,11,21</sup> have been demonstrated as superior alternatives to metals at mid-infrared to THz frequencies. Interestingly, many phonon-resonant materials such as quartz<sup>22</sup>, zinc oxide<sup>23</sup>, calcite<sup>24</sup> and hBN<sup>10,11,21</sup> are natural hyperbolic materials<sup>25–27</sup>. These natural hyperbolic materials support hyperbolic phonon-polariton modes within homogeneous crystals with atomic-scale unit cells, thus the upper limit on the highest propagating wavevectors  $\mathbf{k}$  associated with artificial metal-dielectric HMMs is no longer an issue. Instead, photonic confinement within tiny volumes in the few nanometre range becomes possible. This was recently demonstrated by Dai *et al.*<sup>11</sup> where surface phonon polariton propagation within a three monolayer ( $< 1$  nm) thin flake of hBN was reported. It is the propagation of such high- $\mathbf{k}$  fields that are scattered off or launched from deeply sub-diffractive objects that is at the heart of super-resolution imaging. These benefits are also coupled with a drastic reduction in the optical losses compared with HMMs, which results in improved performance, that is, higher field confinement<sup>10,11</sup> and improved image resolution.

In contrast to HMMs reported to date, hBN offers the additional functionality of sub-wavelength imaging in different spectral regions through the presence of two separate spectral bands (Supplementary Fig. 1) that exhibit inverted hyperbolic response, making this an ideal material for exploring the basic phenomenon of HPs. These two regimes are referred to as the lower and upper Reststrahlen bands<sup>10,11</sup>, where this term refers to the spectral range between the longitudinal and transverse optic phonons of a polar crystal where a negative real part of the

dielectric function is observed. The presence of two bands results from the highly anisotropic crystal structure of hBN, where  $a$ ,  $b$  and  $c$  axis oriented optic phonons are supported and are widely separated in frequency<sup>28</sup>. These two bands not only exhibit hyperbolic behaviour, but the crystal axis featuring negative real permittivity is inverted, thus the lower and upper bands offer Type-I ( $\text{Re}(\epsilon_t) > 0$  and  $\text{Re}(\epsilon_z) < 0$  in  $\sim 760 < \omega < 825 \text{ cm}^{-1}$ ) and Type-II ( $\text{Re}(\epsilon_t) < 0$  and  $\text{Re}(\epsilon_z) > 0$  in  $\sim 1,360 < \omega < 1,610 \text{ cm}^{-1}$ ) hyperbolic response, respectively. The inversion of the signs of the dielectric function results in unusual behaviour, such as a negative (positive)  $z$ -component of the group velocity in the upper (lower) Reststrahlen bands. This results in unique phenomenon such as higher order resonance modes occurring at lower (higher) frequencies. Until now, due to a lack of a homogeneous material exhibiting both types of hyperbolicity, a comprehensive study of the impact of these two unique regimes for nanoimaging and super-resolution focusing have not been experimentally probed, with Caldwell *et al.*<sup>10</sup> providing the only prior study comparing the unique behaviours of these two regimes, albeit within the context of three-dimensionally confined cavities. In addition to providing a homogeneous medium exhibiting both Type I and II hyperbolicity, hBN also exhibits much lower losses (higher efficiencies) than plasmonic materials, with the imaginary part of the dielectric function,  $\text{Im}(\epsilon_t) \sim 0.1$  for  $\text{Re}(\epsilon_t) = -1$  at  $\omega = 1573 \text{ cm}^{-1}$  and  $\text{Im}(\epsilon_z) \sim 0.1$  for  $\text{Re}(\epsilon_z) = -1$  at  $\omega = 809 \text{ cm}^{-1}$ , which is crucial for realizing extended propagation and detection of high- $\mathbf{k}$  polariton modes (deeply sub-diffractive confinement)<sup>10,11,17</sup>.

The dielectric permittivities are also highly dispersive in these two regions, giving rise to a frequency-dependent ratio between  $\epsilon_t$  and  $\epsilon_z$ . Thus, because of the presence of both Type I and II hyperbolicity, from equation (1) we can predict that the propagation angle  $\theta$  will be an increasing (decreasing) function of the frequency in the lower (upper) Reststrahlen bands. As shown in Fig. 1a,b, as the frequency is increased,  $\theta$  increases from about  $16^\circ$  to  $87^\circ$  ( $\Delta\theta \approx 71^\circ$ ) within the Type I lower Reststrahlen band, while it decreases from  $\theta \approx 83^\circ$  to  $\theta \approx 2^\circ$  ( $\Delta\theta \approx 81^\circ$ ) in the Type II upper Reststrahlen band.

Here we experimentally verify this inversion of the propagation angle within the two spectral bands, providing near-field imaging of sub-diffractive objects under a thin slab of hBN. This investigation also enabled the experimental demonstration of the unusual imaging properties of both Type I and II hyperbolic media, thereby providing the physical description necessary to realize and optimize near-field imaging using natural hyperbolic media.

## Results

**Theory and simulations.** This frequency-dependent tuning of the angular HP propagation in hBN and the suitability of this material for near-field imaging can be easily quantified and visualized via two-dimensional (2D) numerical calculations. For this, we consider a  $0.3 \mu\text{m}$  wide gold stripe on a Si substrate with an hBN cover layer (the thickness  $h = 1 \mu\text{m}$ ) illuminated by a  $p$ -polarized plane wave incident from the top. Simulated electric-field distributions ( $|E_z|$ ) at six typical operation frequencies are presented in Fig. 1c–h, and demonstrate the directional nature of the HPs. Here the high- $\mathbf{k}$  fields scattered from the edges of the embedded gold stripe are induced to propagate within the hBN flake (as marked in Fig. 1d), with the angle of propagation being directly dependent upon the frequency of operation. As stated previously<sup>1–4</sup>, in the absence of the hyperbolic dispersion, such high- $\mathbf{k}$  modes would be evanescent (that is, decay rapidly) within the medium. Each edge of the Au stripe excites two sub-diffractive HPs that propagate at the

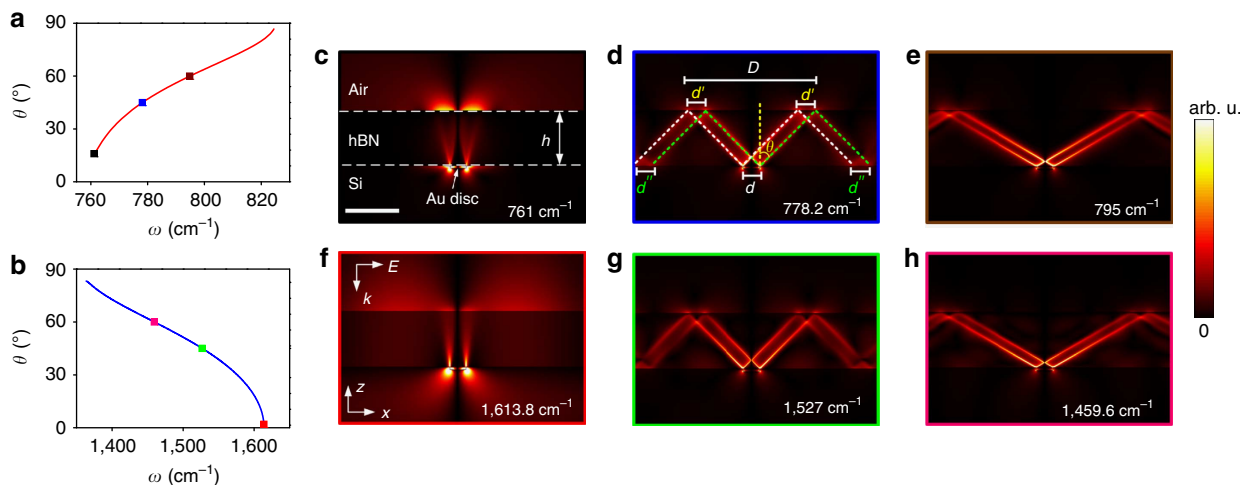


**Figure 1 | Frequency-dependent directional angles of the hyperbolic polaritons propagating inside the hBN.** Solid lines in (a,b) the critical angle  $\theta$  of the HPs as a function of the frequency  $\omega$  in the Type-I ( $760 < \omega < 825 \text{ cm}^{-1}$ ,  $\epsilon_t > 0$  and  $\epsilon_z < 0$ ) and Type-II ( $1,360 < \omega < 1,610 \text{ cm}^{-1}$ ,  $\epsilon_t < 0$  and  $\epsilon_z > 0$ ) hyperbolic bands of the hBN. (c–h) Simulated electric-field distribution ( $|E_z|$ ) at various frequencies. The directional angles evaluated from these simulations are plotted in a,b (colour dots) for comparison:  $\theta = 16^\circ$  (c, at  $\omega = 761 \text{ cm}^{-1}$ ),  $\theta = 2^\circ$  (f, at  $\omega = 1,613.8 \text{ cm}^{-1}$ ),  $\theta = 45^\circ$  (d,g; at  $\omega = 778.2 \text{ cm}^{-1}$  and  $\omega = 1,527 \text{ cm}^{-1}$ ) and  $\theta = 60^\circ$  (e,h; at  $\omega = 795 \text{ cm}^{-1}$  and  $\omega = 1,459.6 \text{ cm}^{-1}$ ). Scale bar,  $1 \mu\text{m}$  (c).

angles  $\pm\theta$ . This frequency dependent propagation angle quantitatively agrees with the analytical predictions based on equation (1) (see Fig. 1a,b), therefore the propagation angle can be predicted via the simple ratio of the extraordinary ( $z$  axis) and ordinary ( $x$ – $y$  plane) components of the anisotropic dielectric function of hBN.

The anticipated super-resolution imaging performance of the hBN slab is directly tied to the propagation angle, as demonstrated in Fig. 1c–h, which as noted above is directly dependent on the type of hyperbolicity. For instance, at wavelengths with very low propagation angles (Fig. 1c,f), the image of the sub-diffraction Au stripe is nearly perfectly restored on the top surface of the hBN, similar to near-field superlensing<sup>29–31</sup>. Namely, the restored width  $d'$  is nearly identical to the actual width  $d$  of the investigated stripe (for example,  $d' \approx 309 \text{ nm}$ , around  $\lambda/40$ -resolution at  $\omega = 778.2 \text{ cm}^{-1}$  or  $\lambda = 12.85 \mu\text{m}$ ). However, as the angle is increased (Fig. 1d,e for the lower and Fig. 1g,h for the upper Reststrahlen bands), an enlarged outline of the object image is obtained with the width  $D(\omega) = d + 2h \tan\theta(\omega)$ . Note that due to the inversion of the dependence of  $\theta$  on  $\omega$  between the two spectral bands, superlensing-type response is observed at low and high frequencies within the lower and upper Reststrahlen bands, respectively, while the enlarged imaging behaviour is observed at high and low frequencies.

This unusual enlargement can be clearly observed in the more practical three-dimensional (3D) cases. As shown in Fig. 2a, the  $0.6\text{-}\mu\text{m}$ -diameter gold disc is once again perfectly restored at very shallow angles; however, at larger propagation angles a double concentric ring-like field distribution is recorded in the near-field (Fig. 2b), rather than a direct replication of the original field distribution of the object. This enlarged pattern results from the frequency-dependent propagation angle of the HPs (cone-like shape for 3D case, see the sketch in Fig. 2c). This unexpected phenomenon is also found for other shapes (like a Au square and stripe) as shown in Fig. 2d–i. Intriguingly, the trace of the HP cones reconstructs the enlarged and slightly distorted pattern that is still able to identify the outline (shape) information of the object. Quantitatively, through recording the HP-reconstructed outline ( $D(\omega)$ ), we can extract the geometric size and shape from the strict relationship of  $D(\omega) = d + 2h \tan\theta(\omega)$ .

These results suggest an interesting HP-based imaging scenario, which will be verified and visualized by our experiments below.

**Experimental results in Type I hyperbolic band.** The predicted imaging mechanism is verified by our experiments first in the Type I hyperbolic band, as presented in Fig. 3. A schematic of the experimental setup is provided in Fig. 3a where the images restored by the hBN layer are recorded using a scattering-type scanning near-field optical microscope (s-SNOM). We use a  $0.15\text{-}\mu\text{m}$ -thick exfoliated hBN flake to image the underlying,  $30 \text{ nm}$  tall, gold nanodiscs with  $0.3\text{-}\mu\text{m}$  diameter and  $1.3\text{-}\mu\text{m}$  centre-to-centre separation. The metallic tip of the s-SNOM is illuminated by a home-built, tunable broadband infrared laser<sup>32,33</sup> with the peak position of the laser spectrum (inset in Fig. 3a) matched to the lower, Type-I hyperbolic region of hBN ( $760 \text{ cm}^{-1} < \omega < 825 \text{ cm}^{-1}$ ). Both the optical and topographic information at the top surface of the hBN layer are collected simultaneously (details in Methods). In the obtained topographic image (Fig. 3b), the gold discs are masked by the covering hBN layer, while in the broadband-SNOM image (Fig. 3c), all three nanodiscs are clearly resolved with bright contrast (that is, high signal-to-background ratio). To ensure that the imaging is indeed due to the hyperbolic nature of the hBN slab, a control image was also collected at a frequency outside of the lower Reststrahlen band using a  $\text{CO}_2$  laser at  $\omega = 952 \text{ cm}^{-1}$ , where both components of the dielectric function are positive ( $\text{Re}(\epsilon_t) = 8.8$  and  $\text{Re}(\epsilon_z) = 2$ ). As shown in Fig. 3e, in contrast to the hyperbolic case, only weak features of the discs are observed through the thin hBN layer in the control experiment. This is further demonstrated by the line profiles taken across the two discs for both cases presented in Fig. 3f, with a marked enhancement in the imaging efficiency observed in the hyperbolic regime. Such an effect would be further amplified within thicker hBN slabs, whereby any structural morphology would be totally lost, but the near-field imaging properties retained. The hyperbolic images also provided a narrower FWHM (full width at half maximum) of about  $0.5 \mu\text{m}$  in addition to the markedly improved contrast (signal-to-background ratio). Considering the resolved deeply

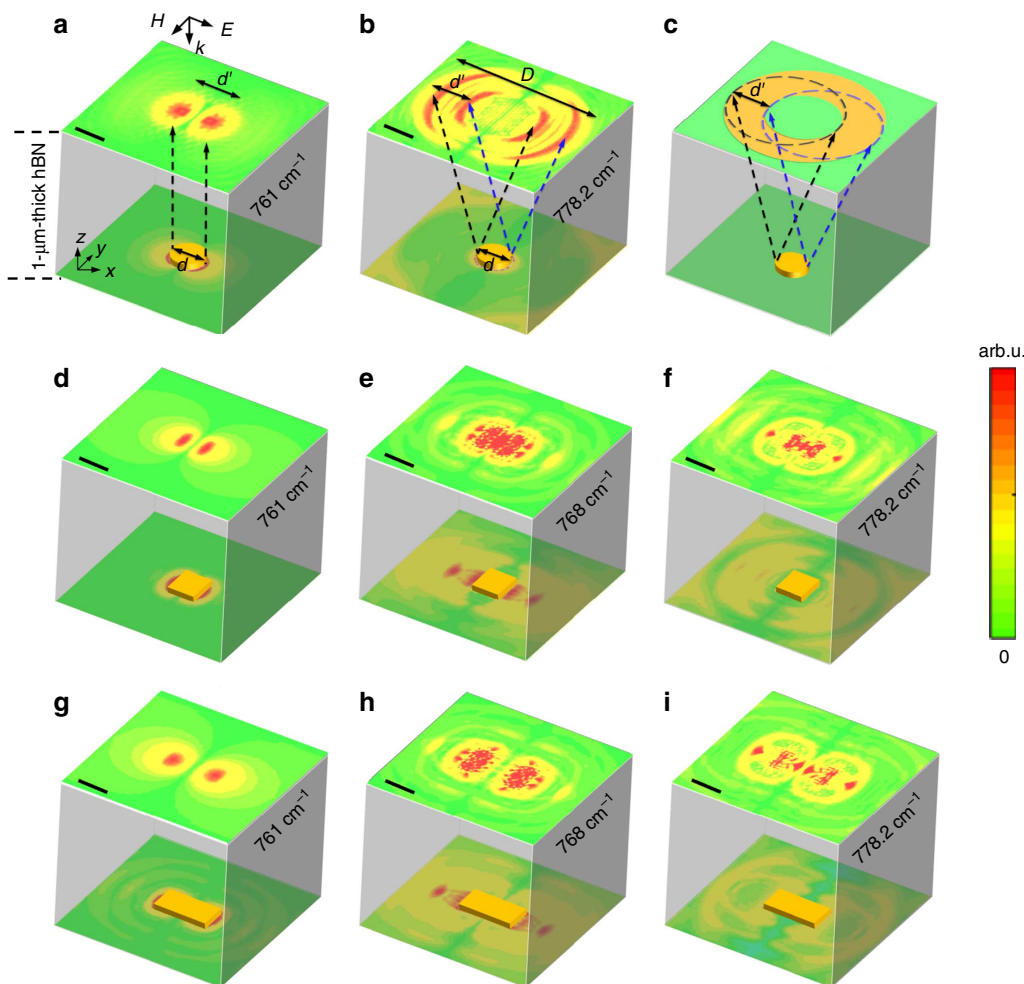


**Figure 2 | Three dimensional simulations of imaging different structures through the hBN layer.** (a,b) 3D simulations of imaging a gold disc (0.6- $\mu\text{m}$  diameter) below the 1- $\mu\text{m}$ -thick hBN layer (scale bars, 0.6  $\mu\text{m}$ ). Simulated electric-field distributions ( $|E_z|$ ) taken at top and bottom surface of the hBN layer for imaging, **a**, at  $\omega = 761 \text{ cm}^{-1}$ . **b**, at  $\omega = 778.2 \text{ cm}^{-1}$  show the frequency-dependent transition between perfect imaging and enlarged imaging. (c) The sketch of the mechanism of the enlargement observed in **b**. (In this sketch we do not consider the influence of the illumination polarization). (d-f)  $|E_z|$ -distributions of imaging a gold square (1- $\mu\text{m}$  length, 50-nm height). (g-i)  $|E_z|$ -distributions of imaging a gold bar (1- $\mu\text{m}$  width, 2- $\mu\text{m}$  length, 50-nm height). All these images show the frequency-dependent transition between perfect imaging and enlarged imaging of the geometric outline of the structures. Scale bars, 1.2  $\mu\text{m}$  (d-i). The z axis in all the images is not to scale for better visualization.

subwavelength optical FWHM ( $\sim \lambda/24$ ), this comparison clearly confirms the improved near-field imaging by the hBN layer.

Although the broadband s-SNOM image shown in Fig. 3c is able to resolve the discs, it does not reflect the actual field distribution of the image due to its detection scheme<sup>33</sup>. Because of the broadband light source used, the detection is not monochromatic as in the simulations presented in Figs 1 and 2. Instead, the collected images are the superposition of all the different frequency components of the broadband laser and therefore the concentric-ring field distributions are not directly observed. Further, depending on the chosen interference phase difference (constructive or destructive phases, involving the position of a reference mirror in our setup, see Methods), it can also show reversed imaging contrasts (see ref. 33). Therefore, the broadband s-SNOM image alone cannot directly reveal the actual image of the field distributions of the discs and the frequency dependence of the hBN layer. For this, monochromatic s-SNOM images would be required; however, currently such sources are not readily available within this spectral range.

To determine the actual imaging response through the hBN layer at each individual wavelength, we performed Fourier transform infrared nanospectroscopy (nano-FTIR)<sup>11,33</sup> along a line scan (dashed line in Fig. 3c) across two discs. At each pixel, nano-FTIR delivers a full infrared spectrum recorded at the spatial resolution of the probing tip ( $\sim 50 \text{ nm}$ ). Thus we obtain s-SNOM signals  $s_2(\omega, x)$  as a function of the frequency  $\omega$  and the spatial position  $x$ <sup>11,16,33</sup>. This hyperspectral imaging allows the extraction of detailed spatial line profiles at various frequencies as shown in Fig. 3g. For frequencies within the lower Reststrahlen but  $\omega > 780 \text{ cm}^{-1}$ , two peaks are observed for each disc (see the typical case at  $\omega = 783 \text{ cm}^{-1}$ ). These peaks (with the typical case at  $\omega = 783 \text{ cm}^{-1}$ ) correspond to the edge-excited HPs. The distance  $D$  between the two edge-launched peaks increases from about 0.4 to  $\sim 1.25 \mu\text{m}$  (for the right disc) when changing the frequency from 780 to  $807 \text{ cm}^{-1}$ , with this distance being directly related to the frequency-dependent HP propagation angle. At frequencies  $\omega < 780 \text{ cm}^{-1}$ , the two edge-launched peaks are not resolved by the hBN layer due to the very small directional angle of HPs, leading to one single broad peak



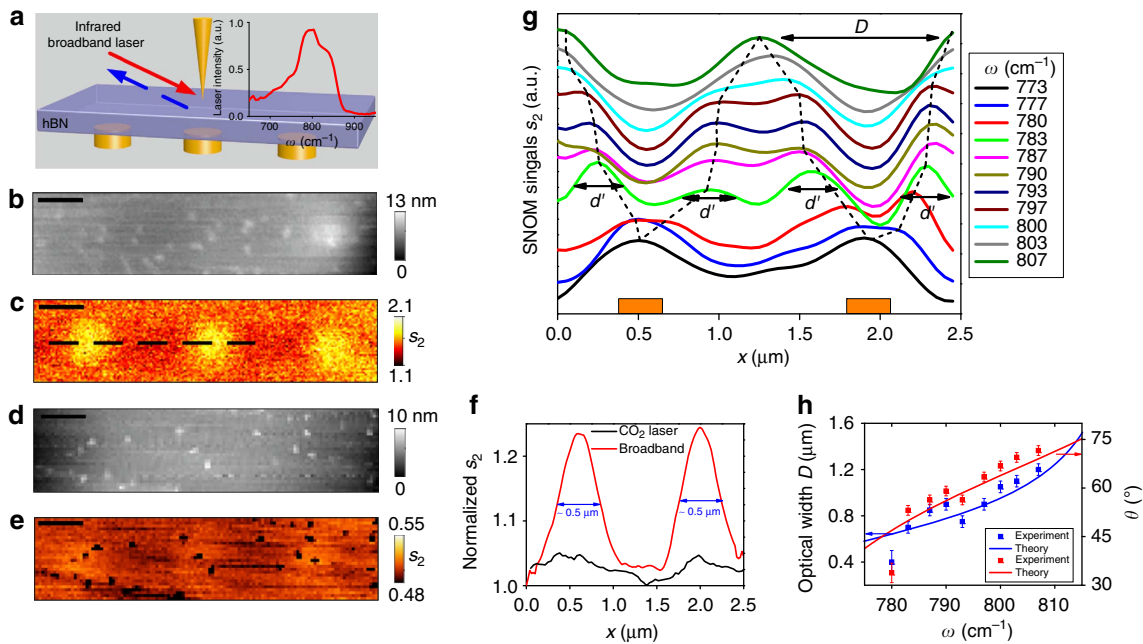


**Figure 3 | Experimental demonstration of super-resolution imaging with tunable hyperbolic polaritons in the Type I band.** (a) Sketch of the experimental setup. The right inset is the normalized laser spectrum of the used mid-infrared broadband laser. The gold nanodiscs are with 0.3- $\mu\text{m}$  diameter and 1.3- $\mu\text{m}$  centre-to-centre separation. (b) The AFM topography taken at the top surface of the 0.15- $\mu\text{m}$ -thick hBN flake. (c) The 2D infrared optical amplitude ( $s_2$ ) images taken with the broadband laser. (d) The control infrared amplitude image taken with a CO<sub>2</sub> laser at  $\omega = 952 \text{ cm}^{-1}$  that is out of the hyperbolic region of the hBN. The small black dots in the image are caused from topographic features (corresponding topographic image shown in (b)). Scale bars, 0.5  $\mu\text{m}$ . (e) Detailed profiles of the s-SNOM signals across two neighbouring discs (along the line marked in (c), averaged over five scan lines) for the cases using the broadband laser (red line) and the CO<sub>2</sub> laser (black line), respectively. Both profiles are normalized to their respective minimum values outside the discs. The broadband imaging shows much stronger contrasts for the discs. (f) Detailed Nano-FTIR line profiles at various frequencies. Dashed line marks the position variations of the peak of edge-launched hyperbolic polaritons. (g) Optical widths and corresponding directional angles of the hyperbolic polaritons evaluated from the experimental results (dots) in comparison with the calculated results (solid lines). The error bars result from the spatial pixel size (50 nm) in nano-FTIR measurements.

observed for each disc. On the basis of the smallest peak-to-peak separation in our results being  $\sim 0.4 \mu\text{m}$  at  $\omega = 780 \text{ cm}^{-1}$  ( $\lambda = 12.8 \mu\text{m}$ ), this corresponds to a sub-diffractive resolution of about  $\lambda/32$  (also see Supplementary Fig. 3).

For the comparison of the theoretically predicted propagation angles (Fig. 1a) and those experimentally derived from the s-SNOM measurements, we plot the experimentally determined  $D$  (blue curve and data) and corresponding directional angles  $\theta$  (red curve and data) of the HPs as functions of  $\omega$  in Fig. 3h. The theoretical result (from  $D(\omega) = d + 2h \tan\theta(\omega)$ ) is also shown for comparison. Good quantitative agreement is found between the experiments and theory. This verifies the predicted tuning range of the propagation angle of the HPs to be about  $35^\circ - 70^\circ$  and the tunable ratio ( $D/d$ ) to range from 1.39 to 4.2. However, certain discrepancies are still found in this comparison, and we do not observe multiple peaks originating from the multireflection of the HPs within the hBN slab.

**Experimental results in Type II hyperbolic band.** To extract the near-field frequency-dependent imaging and HP propagation angles, near-field imaging experiments were also performed in the Type II hyperbolic band by using a line-tunable quantum cascade laser (spanning from 1,310 to 1,430  $\text{cm}^{-1}$ ). This monochromatic laser allows us to present the HP-reconstructed imaging phenomenon in a more intuitive way compared to the case with the broadband laser. First, we performed the s-SNOM measurements to image a Au stripe (about 1- $\mu\text{m}$  long, 100-nm wide, as sketched

in Fig. 4a) that is covered by the 0.15- $\mu\text{m}$  hBN layer (atomic force microscopy (AFM) topography in Fig. 4b). In comparison to the circular confusion caused by the HP cones (circular cross section) for understanding the imaging results. Because the deeply sub-diffractive width ( $< \lambda/70$ ) of the stripe, optical information cannot be recorded at frequencies outside the hyperbolic band, as shown in Fig. 4c. In contrast, we clearly observe enlarged optical patterns formed by the HPs (Fig. 4d–f). Qualitatively, these elliptical, rectangular patterns carry and reflect the shape information of the original object. Quantitatively, from the measured width and length of the patterns, in conjunction with the known HP propagation angle, we can extract the geometric size of the investigated object. Using this approach, we estimate the width of the stripe is about 0.12  $\mu\text{m}$ , and the estimated length is about 1.1  $\mu\text{m}$ , which is consistent with SEM measurements of the stripe prior to hBN exfoliation. We note that for frequencies where HPs have smaller diffractive angles (namely, the HP cone with the very small diameter), the reconstructed image will be similar to the one-to-one near-field superlensing<sup>29–31</sup>. Therefore, in such HP-based imaging phenomenon, it has two frequency-dependent operation modes: the enlarged reconstruction and the one-to-one superlensing.

As previously discussed, we also experimentally demonstrated that the diameter of the HP cone increases with decreasing frequency, which is inverted with respect to the Type I band. These two distinct frequency dependences, found in two spectral regimes through imaging of the sub-diffractive objects, verify

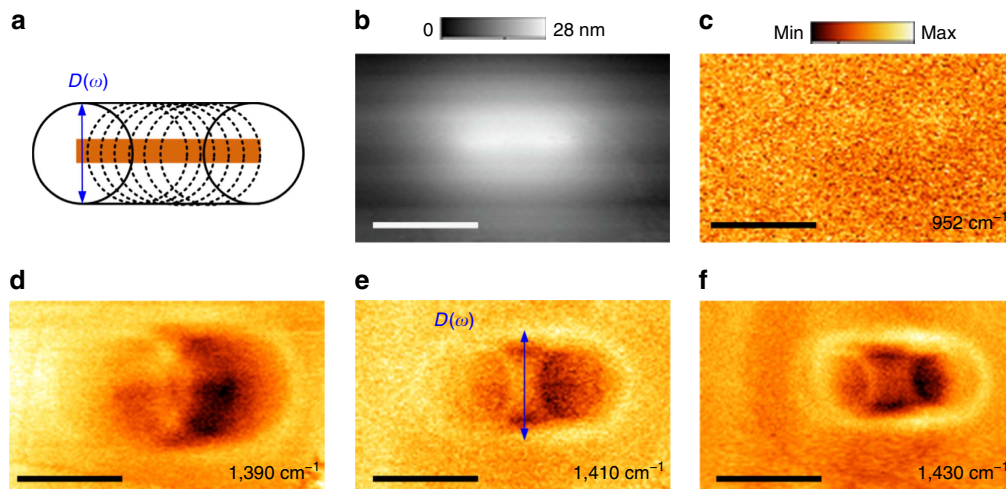


**Figure 4 | Experimental demonstration of enlarged imaging of a Au stripe with tunable HPs in the Type II band.** (a) Sketch of the imaged object—a Au stripe (not to scale), located below the 0.15  $\mu\text{m}$  thick hBN flake. The length  $l$  of the stripe is about 1  $\mu\text{m}$ , and the width  $w$  is around 0.1  $\mu\text{m}$ . The dashed rings result from launched HPs from the edges of the stripe. These HPs form an enlarged outline that reveals the object information. (b) AFM topography taken from the hBN top surface. (c) the s-SNOM amplitude image ( $s_3$ ) taken at  $\omega = 952 \text{ cm}^{-1}$  outside the hyperbolic band. No optical feature is observed from the underlying structure. (d–f) Spectroscopic imaging the stripe in the Type II hyperbolic band. The bright outlines found in the images (amplitude  $s_3$ ) are formed by the HP cones, which are enlarged compared to the original structure. From the measured  $D(\omega)$ , we can estimate the width  $w$  of the stripe (using the relationship  $D(\omega) = w + 2h \tan\theta(\omega)$ ) is about 0.12  $\mu\text{m}$ , and the estimated length is about 1.1  $\mu\text{m}$ . These results verify that from imaging the enlarged outline, we are able to reveal the object information due to the frequency-dependent directivity of HPs. Scale bars, 1  $\mu\text{m}$ .

again that the two types of hyperbolic dispersion exist in the hBN crystal, without the need for fabricating HMM structures.

In addition to the isolated structures, we also investigated periodic arrays of nanostructures. We imaged the arrays of the Au nanodiscs ( $5 \times 5$  array, sketched in Fig. 5a) with different separations. The diameter of the discs was fixed at 0.3  $\mu\text{m}$ . The gap separation between two discs varied from  $g = 0.1 \mu\text{m}$  to  $g = 1 \mu\text{m}$ . The experimental results are shown in Fig. 5d–f. We observed the complicated overlapping of the HP cone launched by each disc. However, with these sub-diffractive HPs, we have the opportunity to distinguish the deeply sub-diffractive structures that are not readily seen in either AFM topography or near-field imaging at frequencies outside of the hyperbolic regime (see the comparison of Fig. 5b–d).

#### HPs for sub-diffractive focusing and selective waveguiding.

In addition to the already proven high-resolution imaging with tunable enlargement of the outline of sub-diffractive objects using only a simple slab of hBN, the highly directional nature of HPs can also result in sub-diffractive focusing behaviour. When imaging the nanodiscs with a large diameter of 0.75  $\mu\text{m}$ , we observe the focusing spot with the width of about 0.175  $\mu\text{m}$  ( $\sim \lambda/40$ ) at  $\omega = 1,420 \text{ cm}^{-1}$  (Supplementary Fig. 4). This is because all the HP cones launched by the nanodisc superimpose into the centre point, leading to the concentration of the light. We also investigate this focusing effect with the broadband laser in the Type I hyperbolic band. However, the obtained results are also the superposition of all the frequency components, which are not intuitive. We also note that this super-focusing effect is independently shown and discussed in ref. 34, which was performed concurrently with the work discussed here.

Both the enlarged imaging and the super-focusing are based on the volume-confined, frequency-dependent propagation angle of HPs in hBN. We can envision other potential disruptive technologies based on the great potential of the highly directional HPs. First, this frequency-selective waveguiding could be useful

for photonic switching or computing, infrared filtering, or various other nanophotonic applications (Supplementary Fig. 5a, b). Another potential application is realized in the form of an ultracompact subwavelength spectrometer (Supplementary Fig. 5c,d). A natural hBN layer should allow for the spatial separation or filtering of incoming broadband light into different wavelength channels, much like a grating, which could then be detected by subwavelength infrared detector pixels. This particular spectrometer configuration could also be used for chemical and biological detection schemes, in the form of spatially resolved infrared spectroscopy. Under broadband mid-infrared illumination the HPs could carry the vibration (or absorption) information of molecules in contact with the surface, dispersing the spectral information at different angles, enabling them to be spatially resolved by a near-field intensity detector (like the s-SNOM tip) without the need of spectrometers.

#### Discussion

Our work along with that of ref. 34, demonstrate the complete hyperbolic imaging response of hBN and its potential for improving the near-field imaging of deeply embedded objects<sup>35,36</sup> in both the Type I lower and Type II upper Reststrahlen bands, respectively. More specifically, we reveal the hyperbolic nature of the hBN layer for near-field waveguiding, imaging, focusing and its dependence on the operational frequency. Although all our results are restricted in the near field, we also expect that these intriguing findings will benefit far-field imaging by introducing specific geometric designs, such as circular or wedge-shaped hyperlenses<sup>2,3</sup>. Furthermore, as a van der Waals crystal<sup>37</sup>, hBN lends itself to incorporation on non-planar and flexible substrates more amenable to true hyperlensing methodologies<sup>4</sup>. The realization of a naturally occurring, Type I and II hyperbolic media enable various opportunities for nanophotonics that go beyond sub-diffractive near-field imaging and potential hyperlensing. Due to the similar material anisotropy present in other polar dielectric

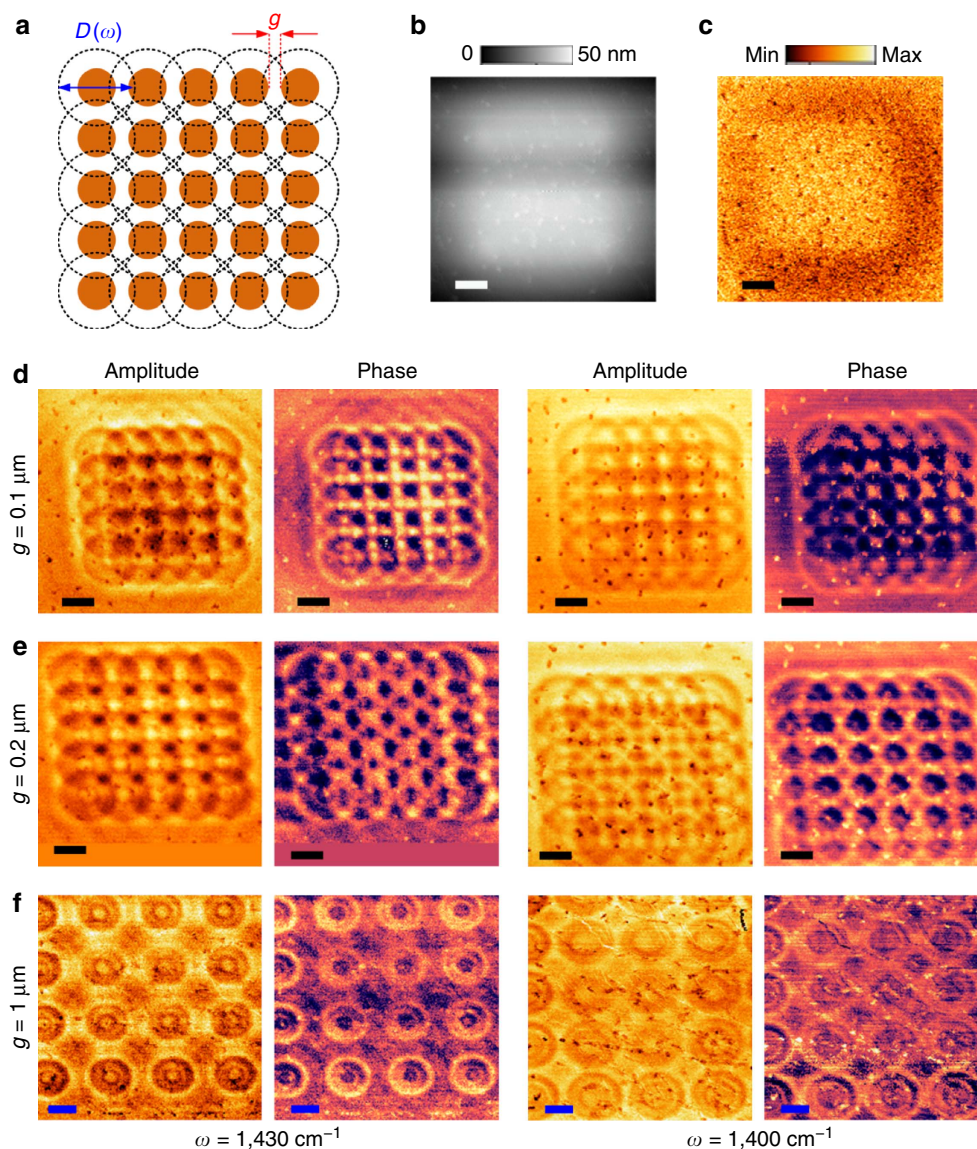


**Figure 5 | Experiments of imaging the arrays of Au nanodiscs with hyperbolic polaritons in the Type II band.** (a) Sketch of the arrays of the Au nanodiscs, located below the 0.15  $\mu\text{m}$  thick hBN flake. The diameter of the discs is fixed to be 300 nm. The gap separation between two discs varies from  $g = 0.1 \mu\text{m}$  to  $g = 1 \mu\text{m}$ . The dashed rings indicate the launched hyperbolic polaritons. (b) The AFM topography of the array with  $g = 0.1 \mu\text{m}$ , taken from the hBN top surface. (c) The s-SNOM image of the array with  $g = 0.1 \mu\text{m}$  taken at  $\omega = 952 \text{ cm}^{-1}$  outside the hyperbolic band. No detailed optical feature is probed for resolving the structure. (d-f) Near-field images (amplitude  $s_3$  and phase  $\phi_3$ ) of the arrays at two different frequencies of 1,430 and 1,400  $\text{cm}^{-1}$  inside the Type II hyperbolic band. Obviously, the launched HPs help to reveal the arrays. In (e) colour spaces are added in the amplitude and phase images taken at 1,430  $\text{cm}^{-1}$ , for keeping the square shape. Scale bars, 0.5  $\mu\text{m}$ .

van der Waals crystals<sup>37</sup>, such as  $\text{MoS}_2$  or  $\text{WS}_2$ , the natural hyperbolic response of hBN may be general to the entire class of polar 2D crystals, thus expanding the potential spectral range of this behaviour from the mid-infrared into the single-digit terahertz spectral region<sup>17,24</sup>.

## Methods

**Sample preparation.** The gold nanostructures used for the near-field experiments were fabricated on a 1- $\mu\text{m}$ -thick intrinsic silicon substrate using electron beam lithography into a bilayer PMMA (poly(methylmethacrylate)) resist. The nanostructures varied in size from 0.2–1  $\mu\text{m}$  in diameter and in arrays with 0.1–1  $\mu\text{m}$  edge-to-edge gaps. A standard liftoff procedure was used following the thermal evaporation of Cr (5 nm)/Au (30 nm) metallization.

hBN crystals were grown using the high-pressure/high-temperature method<sup>38,39</sup>. The standard exfoliation process was used to randomly deposit hBN flakes of various thicknesses onto a PMMA/PMGI (polydimethyl glutarimide) bilayer spun on a

separate silicon substrate. Here the PMMA layer played the role of the flake carrier membrane and the PMGI served as a sacrificial lift-off layer later dissolved by tetramethyl ammonium hydroxide (TMAH) solution (MICROPOSIT MF-319). AFM was utilized to select specific flakes with both sufficient thickness and lateral size for the imaging experiments. The PMMA carrier membrane with an appropriate hBN flake was lifted-off from the substrate and put onto the supportive metal ring held by a home-made micromanipulator. With the help of the micromanipulator, the hBN flake was aligned and transferred face down onto the predefined gold nanostructure by releasing the carrier membrane from the metal ring. Following the transfer, the sample with the carrier membrane on was heated to 130  $^\circ\text{C}$  for about 10 min to soften the PMMA membrane and improve the adhesion of hBN to the underlying nanostructures and silicon substrate. After that the carrier membrane was dissolved in acetone leaving the hBN flake covering the entire array of nanostructures. To improve the adhesion, an ultrasonic clean in acetone and isopropyl alcohol with subsequent oxygen plasma clean was performed on the silicon substrate before the hBN transfer. More details of this transfer technique are given in ref. 40.



**Infrared s-SNOM measurements.** An s-SNOM (commercially available, Neaspec GmbH) system was used to simultaneously measure the optical near fields and topography. The laser system used in Type I hyperbolic band was developed by the Fraunhofer ILT<sup>32,33</sup>. It consists of a commercially available picosecond-laser as the pump source and two subsequent nonlinear converter steps to cover the mid-infrared range. The peak wavelength is continuously tunable from  $\omega = 625 \text{ cm}^{-1}$  ( $\sim 16 \mu\text{m}$ ) to  $\omega = 1,100 \text{ cm}^{-1}$  ( $\sim 9 \mu\text{m}$ ) with bandwidths of some tens to more than hundred wavenumbers. At a repetition rate of 20 MHz and pulse duration of 10 ps, the system provides an average power of up to 10 mW. To address the lower Type-I hyperbolic region of the hBN, the peak position of the laser spectrum in our measurements was set to be at around  $\omega = 790 \text{ cm}^{-1}$  ( $12.7 \mu\text{m}$ ) with a FWHM of about  $90 \text{ cm}^{-1}$ . To suppress the far-field background contribution and solely measure the near-field contribution, the optical signal was demodulated at higher harmonics ( $n\Omega$ ) of the oscillation frequency ( $\Omega \sim 270 \text{ kHz}$ ) of the cantilever (in our cases,  $n = 2$  for the broadband s-SNOM). Nano-FTIR spectra were obtained by constantly moving the mirror in the reference arm of the Michelson interferometer, recording the resulting interferograms and their corresponding complex Fourier transformation<sup>11,33</sup>. In contrast to conventional far-field FTIR, this setup allows to record spectral information with a spatial resolution of down to several tens nm. For 2D imaging, the position of the reference mirror was fixed to be at the position about  $\lambda/8$  away from the maximum of the interference signals. This allows for a visualization of even small spectral changes<sup>31</sup>. The extracted line profiles shown in Fig. 3g were numerically smoothed by using a fast Fourier transform smoothing with three adjacent pixels. This smoothing does not improve the resolution, but rather leads to a conservative estimation of resolution (details in Supplementary Figs 2 and 3). The monochromatic quantum cascade laser used in the Type II band (Figs 4 and 5) is commercially available from Daylight Solutions. The demodulation order  $n = 3$  is chosen for the monochromatic s-SNOM imaging. Near-field optical amplitude ( $s_n$ ) and phase ( $\phi_n$ ) are separated with an interferometric setup<sup>11,19</sup>.

**Numerical simulations.** 2D simulations (Fig. 1) were carried out by the finite-element software COMSOL Multiphysics. A plane-wave illumination was set by using scattering boundary condition. The surrounding boundaries used perfectly matched layer absorbing boundary conditions. 3D simulations (Fig. 2) were done by using CST Microwave Studio. Open boundary conditions were used. We also checked different mesh sizes to make sure that all the simulations reach proper convergence. The dielectric data of hBN used in all the simulations are extracted from far-field FTIR measurements<sup>10</sup>.

## References

- Poddubny, A., Iorsh, I., Belov, P. & Kivshar, Y. Hyperbolic metamaterials. *Nat. Photon.* **7**, 948–957 (2013).
- Jacob, Z., Alekseyev, L. V. & Narimanov, E. Optical hyperlens: far-field imaging beyond the diffraction limit. *Opt. Express* **14**, 8247–8256 (2006).
- Salandrino, A. & Engheta, N. Far-field subdiffraction optical microscopy using metamaterial crystals: theory and simulations. *Phys. Rev. B* **74**, 075103 (2006).
- Liu, Z., Lee, H., Xiong, Y., Sun, C. & Zhang, X. Far-field optical hyperlens magnifying sub-diffraction-limited objects. *Science* **315**, 1686 (2007).
- Hoffman, A. J. *et al.* Negative refraction in semiconductor metamaterials. *Nat. Mater.* **6**, 946–950 (2007).
- Yao, J. *et al.* Optical negative refraction in bulk metamaterials of nanowires. *Science* **321**, 930 (2008).
- Krishnamoorthy, H. N. S., Jacob, Z., Narimanov, E., Kretzschmar, I. & Menon, V. M. Topological transitions in metamaterials. *Science* **336**, 205–209 (2012).
- Ishii, S., Kildishev, A. V., Narimanov, E., Shalaev, V. M. & Drachev, V. P. Sub-wavelength interference pattern from volume plasmon polaritons in a hyperbolic medium. *Las. Photon. Rev.* **7**, 265–271 (2013).
- Yang, X., Yao, J., Rho, J., Yin, X. & Zhang, X. Experimental realization of three-dimensional indefinite cavities at the nanoscale with anomalous scaling laws. *Nat. Photon.* **6**, 450–454 (2012).
- Caldwell, J. D. *et al.* Sub-diffraction, volume-confined polaritons in the natural hyperbolic material: hexagonal boron nitride. *Nat. Commun.* **5**, 5221 (2014).
- Dai, S. *et al.* Tunable phonon polaritons in atomically thin van der Waals crystals of boron nitride. *Science* **343**, 1125–1129 (2014).
- Prokes, S.M. *et al.* Hyperbolic and plasmonic properties of silicon/Ag aligned nanowire arrays. *Opt. Express* **21**, 14962–14974 (2013).
- Khurgin, J. B. & Boltasseva, A. Reflecting upon the losses in plasmonics and metamaterials. *MRS Bull.* **37**, 768–779 (2012).
- West, P. R. *et al.* Searching for better plasmonic materials. *Las. Photon. Rev.* **4**, 795–808 (2010).
- Tassin, P., Koschny, T., Kafesaki, M. & Soukoulis, C. M. A comparison of graphene, superconductors and metals as conductors for metamaterials and plasmonics. *Nat. Photon.* **6**, 259–264 (2012).
- Hillenbrand, R., Taubner, T. & Keilmann, F. Phonon-enhanced light-matter interaction at the nanometre scale. *Nature* **418**, 159–162 (2002).
- Caldwell, J. D. *et al.* Low-loss, infrared and terahertz nanophotonics using surface phonon polaritons. *Nanophotonics* **4**, 44–68 (2015).
- Caldwell, J. D. *et al.* Low-loss, extreme sub-diffraction photon confinement via silicon carbide surface phonon polariton nanopillar resonators. *Nano Lett.* **13**, 3690–3697 (2013).
- Wang, T., Li, P., Hauer, B., Chigrin, D. N. & Taubner, T. Optical properties of single infrared resonant circular microcavities for surface phonon polaritons. *Nano Lett.* **13**, 5051–5055 (2013).
- Chen, Y. *et al.* Spectral tuning of localized surface phonon polariton resonators for low-loss mid-ir applications. *ACS Photon.* **1**, 718–724 (2014).
- Xu, X. G. *et al.* One-dimensional surface phonon polaritons in boron nitride nanotubes. *Nat. Commun.* **5**, 4782 (2014).
- Da Silva, R. E. *et al.* Far-infrared slab lensing and subwavelength imaging in crystal quartz. *Phys. Rev. B* **86**, 155152 (2012).
- Fonoberov, V. A. & Balandin, A. A. Polar optical phonons in wurtzite spheroidal quantum dots: theory and application to ZnO and ZnO/MgZnO nanostructures. *J. Phys. Condens. Matter* **17**, 1085–1097 (2005).
- Thompson, D. W., De Vries, M. J., Tiwald, T. E. & Woollam, J. A. Determination of optical anisotropy in calcite from ultraviolet to mid-infrared by generalized ellipsometry. *Thin Solid Films* **313**, 341–346 (1998).
- Sun, J., Litchinitser, N. M. & Zhou, J. Indefinite by nature: from ultraviolet to terahertz. *ACS Photon.* **1**, 293–303 (2014).
- Zhang, Y., Fluegel, B. & Mascarenhas, A. Total negative refraction in real crystals for ballistic electrons and light. *Phys. Rev. Lett.* **91**, 157404 (2003).
- Chen, X. L., He, M., Du, Y. X., Wang, W. Y. & Zhang, D. F. Negative refraction: an intrinsic property of uniaxial crystals. *Phys. Rev. B* **72**, 113111 (2005).
- Geick, R., Perry, C. H. & Rupprecht, G. Normal modes in hexagonal boron nitride. *Phys. Rev. B* **146**, 543–547 (1966).
- Pendry, J. B. Negative refraction makes a perfect lens. *Phys. Rev. Lett.* **85**, 3966–3969 (2000).
- Fang, N. *et al.* Sub-diffraction-limited optical imaging with a silver superlens. *Science* **308**, 534–537 (2005).
- Taubner, T., Korobkin, D., Urzhumov, Y., Shvets, G. & Hillenbrand, R. Near-field microscopy through a SiC superlens. *Science* **313**, 1595 (2006).
- Wueppen, J., Jungbluth, B., Taubner, T. & Loosen, P. Ultrafast tunable mid IR source. in *Infrared, Millimeter and Terahertz Waves (IRMMW-THz)*, 36th International Conference, IEEE, 1–2 (2011).
- Bensmann, S. *et al.* Near-field imaging and spectroscopy of locally strained GaN using an IR broadband laser. *Opt. Express* **22**, 22369–22381 (2014).
- Dai, S. *et al.* Subdiffractional focusing and guiding of polaritonic rays in a natural hyperbolic material. *Nat. Commun.* **6**, 6963 (2015).
- Taubner, T., Keilmann, F. & Hillenbrand, R. Nanoscale-resolved subsurface imaging by scattering-type near-field optical microscopy. *Opt. Express* **13**, 8893–8899 (2005).
- Li, P., Wang, T., Bockmann, H. & Taubner, T. Graphene-enhanced infrared near-field microscopy. *Nano Lett.* **14**, 4400–4405 (2014).
- Geim, A. K. & Grigorieva, I. V. Van der Waals heterostructures. *Nature* **499**, 419–425 (2013).
- Taniguchi, T. & Watanabe, K. Synthesis of high-purity boron nitride single crystals under high pressure by using Ba-BN solvent. *J. Cryst. Growth* **303**, 525–529 (2007).
- Watanabe, K., Taniguchi, T. & Kanda, H. Direct-bandgap properties and evidence for ultraviolet lasing of hexagonal boron nitride single crystal. *Nat. Mater.* **3**, 404–409 (2004).
- Kretinin, A. V. *et al.* Electronic Properties of graphene encapsulated with different two-dimensional atomic crystals. *Nano Lett.* **14**, 3270–3276 (2014).

## Acknowledgements

This work was supported by the Excellence Initiative of the German federal and state governments, the Ministry of Innovation of North Rhine-Westphalia, the DFG under SFB 917 and the Korean Defense Acquisition Program Administration and the Agency for Defense Development as a part of a basic research program under the contract UD110099GD. Funding for J.D.C. was provided by the Office of Naval Research and administered by the NRL Nanoscience Institute and was carried out at the University of Manchester through the NRL Long-Term Training (Sabbatical) Program. A.K. and K.S.N. acknowledge support from the Engineering and Physical Sciences Research Council (UK), The Royal Society (UK), European Research Council and EC-FET European Graphene Flagship. P.L. and Th.T. thank G. von Plessen and D. Chigrin for valuable comments and the proofreading.

## Author contributions

P.L., J.D.C., Th.T. and K.S.N. conceived the original ideas. P.L. performed the s-SNOM measurements and numerical simulations. M.L. and F.G. performed the broadband s-SNOM measurements. A.V.K. and J.D.C. fabricated the samples with hBN-covered Au



structures. K.W. and T.T. grew the hBN crystals used in the experiment. P.L, J.D.C. and Th.T. wrote the manuscript. The project was supervised by J.D.C, Th.T. and K.S.N.

### Additional information

**Supplementary Information** accompanies this paper at <http://www.nature.com/naturecommunications>

**Competing financial interests:** The authors declare no competing financial interests.

**Reprints and permission** information is available online at <http://npg.nature.com/reprintsandpermissions/>

**How to cite this article:** Li, P. *et al.* Hyperbolic phonon-polaritons in boron nitride for near-field optical imaging and focusing. *Nat. Commun.* 6:7507 doi: 10.1038/ncomms8507 (2015).



This work is licensed under a Creative Commons Attribution 4.0 International License. The images or other third party material in this article are included in the article's Creative Commons license, unless indicated otherwise in the credit line; if the material is not included under the Creative Commons license, users will need to obtain permission from the license holder to reproduce the material. To view a copy of this license, visit <http://creativecommons.org/licenses/by/4.0/>